Use of the Grand Canonical Transition-Matrix Monte Carlo Method to Model Gas Adsorption in Porous Materials*

Daniel W. Siderius† and Vincent K. Shen

Chemical Sciences Division, National Institute of Standards and Technology, Gaithersburg, Maryland 20899, USA

(Dated: November 30, 2017)

Abstract

We present grand canonical transition-matrix Monte Carlo (GC-TMMC) as an efficient method for simulating gas adsorption processes, with particular emphasis on subcritical gas adsorption in which capillary phase transitions are present. As in other applications of TMMC, the goal of the simulation is to compute a particle number probability distribution (PNPD), from which thermophysical properties of the system can be computed. The key advantage of GC-TMMC is that, by appropriate use of histogram reweighting, one can generate an entire adsorption isotherm, including those with hysteresis loops, from the PNPD generated by a single GC-TMMC simulation. We discuss how to determine various thermophysical properties of an adsorptive system from the PNPD, including the identification of capillary phases and capillary phase transitions, the equilibrium phase transition, other free energies, and the heat of adsorption. To demonstrate the utility of GC-TMMC for studies of adsorption, we apply the method to various systems including cylindrical pores and a crystalline adsorbent to compute various properties and compare results to previously published data. Our results demonstrate that the GC-TMMC method efficiently yields adsorption isotherms and high-quality properties of adsorptive systems and can be straightforwardly applied to more complex fluids and adsorbent materials.

Keywords: molecular simulation, confined fluid, hysteresis, phase equilibrium, thermodynamic stability, new keyword

I. INTRODUCTION

As a general rule, the properties of a fluid can be altered significantly from their bulk values when confined in tight spaces, with the magnitude of such alterations dependent on the characteristics of the confining walls, specifically, the affinity of the fluid to the surface[1]. Of particular scientific and technical interest is the effect of confinement on a fluid's phase behavior (or phase boundaries)[1–3]. For example, fluid adsorption in porous materials, the focus of this work, serves as the basis for potential viable carbon capture technologies[4–7]. While theory and simulation have played a historically significant role in the characterization of porous materials[1,8,9], they have more recently been identified as key tools in screening and developing potential carbon capture materials[10–12]. Thus, the advancement of carbon capture technologies and other applications of gas adsorption will depend on the availability and further development of computationally efficient and precise methods to predict the thermodynamic and dynamic properties of fluids in porous materials. At present, the two primary molecular modeling tools used in studies of adsorption are density functional theory[13] (with which we include the closely related lattice mean field theories[14–17]) and various forms of Monte Carlo (MC) molecular simulation[18,19]. These methods have proven essential to the advancement of the fundamental understanding of adsorption processes[8] by, for example, suggesting the existence of cavitation-induced capillary evaporation in ink-bottle pores prior to its observance experimentally[20] and confirming the relationship between subcritical adsorption hysteresis and fluid metastability[21,22].

II. GRAND CANONICAL TRANSITION-MATRIX MONTE CARLO METHOD

We begin by presenting some important details of the GC-TMMC simulation algorithm that we aim to introduce for application in simulation of adsorption hysteresis. TMMC traces back to a method originally introduced by Fitzgerald et al.[23,24], though we use a modified form of TMMC pioneered by Errington and co-workers; for a full discussion of the method, consult Refs 25–30. The main difference between the two variants of TMMC is Errington's incorporation of a biasing function (see below) that improves sampling of unlikely configurations.

The main objective of a GC-TMMC simulation is to calculate the particle number prob-

ability distribution, $\Pi(N;\mu,V,T)$, which is the probability of observing N particles (or atoms or molecules depending on the simulated species) in an ensemble of volume V at fixed temperature T and chemical potential μ. he set of configurations with their number of particles equal to N is said to comprise a macrostate within the ensemble, and the macrostate probability or PNPD in the GC ensemble is given by

$$\Pi(N;\mu,V,T) = \frac{\exp(\beta\mu N)\, Q(N,V,T)}{\Xi(\mu,V,T)}. \tag{1}$$

$Q(N,V,T)$ and $\Xi(\mu,V,T)$ are the canonical and grand canonical partition functions, respectively, $\beta = 1/k_BT$ (in which k_B is Boltzmann's constant[31]), and all other terms are as previously defined. In a conventional grand canonical Monte Carlo (GCMC) simulation, this distribution can be determined by constructing a histogram. In contrast, TMMC utilizes statistics regarding attempted transitions to determine $\Pi(N;\mu,V,T)$. This is done by accumulating information within a collection matrix $\mathbf{C}$ according to

$$\begin{aligned} C(N_o \to N_n) &= C(N_o \to N_n) + p_{\text{acc}}(o \to n) \\ C(N_o \to N_o) &= C(N_o \to N_o) + 1 - p_{\text{acc}}(o \to n) \end{aligned} \tag{2}$$

where the labels o and n identify the old and new configurations for the attempted transition and p_{acc} is the acceptance probability for the attempted transition. The collection matrix $\mathbf{C}$ is updated (see eq 2) after each MC trial move, regardless of whether the move is actually accepted. In GC-TMMC, one usually restricts the simulation to three types of single-molecule trial moves: translations, insertions, and deletions. Thus, the $\mathbf{C}$ matrix is triply banded, i.e., the only possible transitions are $N \to N + \delta$, where $\delta = -1$, 0, or $+1$. The acceptance probability of a trial move may be written as[32,33]

$$p_{\text{acc}}(o \to n) = \min\left[1, \frac{\alpha(n \to o)\,\pi_n}{\alpha(o \to n)\,\pi_o}\right], \tag{3}$$

where $\alpha(o \to n)$ is the probability of generating configuration n from configuration o and π_o is the probability of configuration o. We have written the term p_{acc} in eq 3 as generically as possible so that it can accommodate any type of Monte Carlo move consistent with the chosen ensemble constraints.

Here is a new paragraph in the methods section.

III. EXAMPLE APPLICATIONS

Having established a methodology for using GC-TMMC to obtain adsorption isotherms, we can now turn to some example applications to demonstrate and validate its use. The following examples apply the GC-TMMC method discussed in Sec II to the three adsorptive systems described above.

A. Ar - MWCNT (1)

To begin, we present a series of results for Ar-MWCNT systems to demonstrate how to generate an adsorption isotherm using GC-TMMC. Figure AAa contains the PNPD generated by GC-TMMC simulation of Ar in a MWCNT of inner radius 3.935 nm with axial length $6\sigma_{Ar}$ at $T = 87.3\ K$. The radius corresponds to that of a (58,58) carbon nanotube[34] and the temperature is the normal boiling temperature of Ar, which is also the standard temperature for use of Ar in porous materials characterization[3]. For this demonstration of GC-TMMC, we truncated and linear-force-shifted the fluid-fluid potential at $r_{cut} = 2.5\sigma_{Ar}$[18] and ran the base simulation at the reduced activity $z\sigma_{Ar}^3 = \exp(\beta\mu) / (\Lambda/\sigma_{Ar})^3 = 0.02705$ (Λ is the thermal de Broglie wavelength), corresponding to the reduced pressure $p/p_0 = 12.67$ (far into the liquid state of the bulk fluid at this temperature). The high activity aided sampling of high-N macrostates in the TMMC simulation. Macrostate bounds for the simulation were set to $N_{min} = 0$ and $N_{max} = 2080$ and a short test simulation confirmed that this N_{max} was sufficiently large to yield a low probability tail in Π. Figure XXb contains PNPDs for the same system at various reduced pressures below the bulk saturation pressure, p_0, and Fig XX contains the PNPDs corresponding to the capillary and equilibrium phase transitions. From these PNPDs, and using the phase identification procedure described above, we computed the isotherm shown in Fig YY, where the symbols were obtained from the PNPDs in Fig XXb. The remainder of the isotherm, shown by a black line, is the locus of densities generated by reweighting Π to 1000 different μ statepoints. For this case, we have plotted the average pore density based on the total volume definition of ρ. The bottom panel of Fig TT displays the grand free energy of the system and the equilibrium phase transition is identified by a small arrow. For this particular system, the equilibrium phase transition occurs at $p/p_0 = 0.7568$.

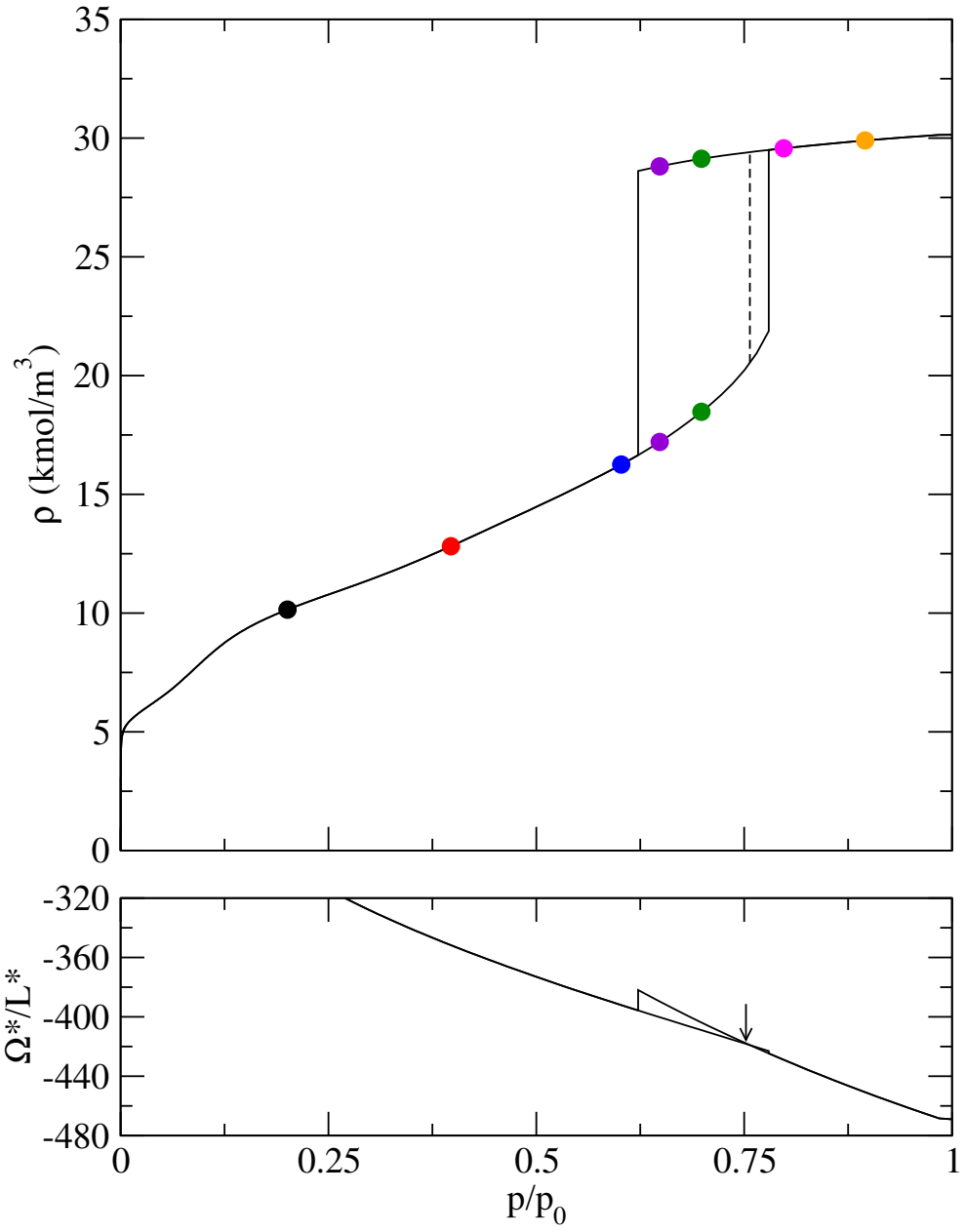

FIG. 1: (Top) Adsorption isotherm for the Ar-MWCNT system with radius 3.935 nm and length 2.043 nm at $T = 87.3$ K. Solid circles indicate the state points at $p/p_0 = 0.20$, 0.40, 0.60, 0.65, 0.70, 0.80, and 0.90, and the color codes match those in Fig XXb. p_0 is the bulk saturation pressure. The solid black line is the locus of adsorbed densities computed by histogram reweighting of $\ln \Pi$ at 1000 μ points. The dashed black line identifies the equilibrium phase transition. (Bottom) Grand free energy per unit length for the same Ar-MWCNT system, in reduced units. The small arrow indicates the equilibrium phase transition, where the grand free energies of the vapor and liquid phases are equal, in this case $p/p_0 = 0.7568$.

In addition to the 3.935 nm MWCNT system, we performed GC-TMMC simulations for Ar-MWCNT systems for four additional inner radii: 1.357, 2.036, 2.646, and 3.053 nm. [These radii correspond to (20,20), (30,30), (39,39), and (45,45) carbon nanotubes[34], respectively.] The axial length was $12\sigma_{Ar}$ for the two smallest radii and $6\sigma_{Ar}$ for the other radii. All simulations were run at $z\sigma_{Ar}^3 = 0.02705$ (as before) and sampled from $N_{min} = 0$ to an N_{max} value that yielded a maximum reduced density of about 0.90. The resultant isotherms, along with that from the 3.935 nm radius system, are shown in Fig 2. Similar to the isotherm for 3.935 nm, the isotherms for 2.646 nm and 3.053 nm are the standard type IV isotherms expected for subcritical adsorption in mesopores with relatively strong fluid-solid interactions. The two smallest radii, however, do not exhibit hysteresis, from which we can conclude that the critical diameter for this system at 87.3 K is between 2.036 nm and 2.646 nm. (Alternatively, the critical hysteresis temperature is below 87.3 K for the smallest radii.) In all five cases shown, a complete monolayer forms at low pressure (approximately $p/p_0 = 0.001$, as determined from a log-scale plot). For the smallest radii, a succession of additional layers forms as pressure increases, until the pore is virtually filled at $p/p_0 = 0.3$. For the remaining sizes, the pores infill slowly until a liquid-like density is reached via a continuous transition (for the 2.036 nm pore) or capillary condensation. In this particular model, the isotherms do not exhibit "steps" that are indicative of the formation of successive monolayers on a smooth, homogeneous surface. This is a consequence of our choice of r_{cut}. Use of a longer cutoff radius such as $4\sigma_{Ar}$ restored the formation of distinct monolayers. Lastly, the equilibrium phase transitions for the three largest radii appear very close to the capillary condensation step. This too was a consequence of the small cutoff radius. We note that these results (along with those in Figs 4 and 5) demonstrate the value of using rigorous calculations to locate the equilibrium phase transition. One may be tempted to estimate its position at the midpoint between the two limits of stability, but our results indicate that such an expectation may prove incorrect.

To further illustrate the utility of GC-TMMC for computing adsorption quantities (or properties) for systems with hysteresis, we now examine the isosteric heat of adsorption for the MWCNT pores discussed above. Historically, the quality of computational calculations of Q_{st} has been much poorer than that of an isotherm, most likely due to greater challenge of computing fluctuation quantities. GC-TMMC, on the other hand, may provide higher quality calculations of fluctuation quantities, since the necessary ensemble averages are computed

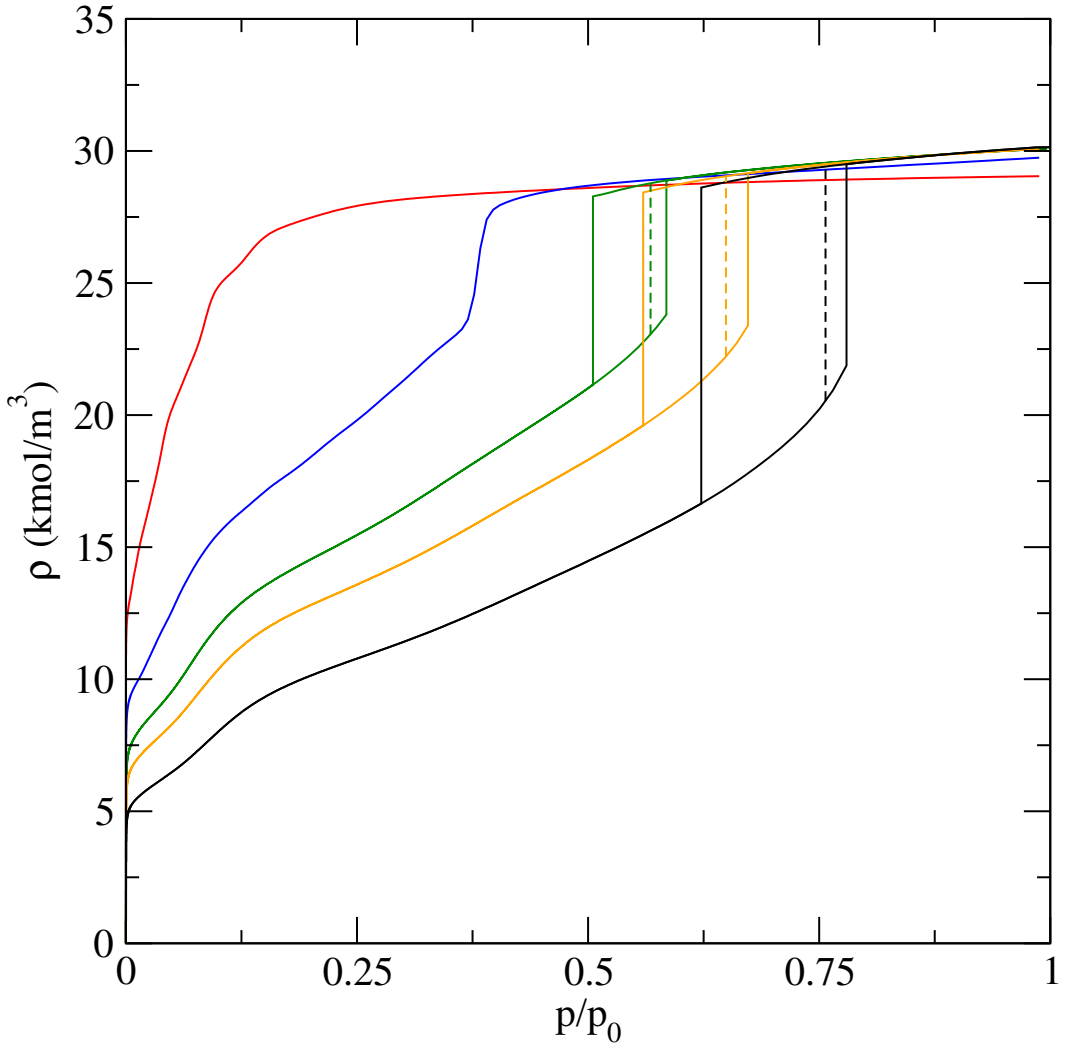

FIG. 2: Adsorption isotherms for Ar-MWCNT systems with radius 1.357 nm (red), 2.036 nm (blue), 2.646 nm (green), 3.053 nm (orange), and 3.935 nm (black), computed at 87.3 K using the GC-TMMC method described in the text. ρ is the average volume of Ar in the pore, based on the total volume definition and p is the gas pressure. p_0 is the bulk saturation pressure for the specified temperature. The equilibrium phase transition for systems exhibiting hysteresis is shown by a dashed line of the same color as the isotherm.

indirectly via the PNPD. Figure 3 contains Q_{st} calculations for the Ar-MWCNT systems whose isotherms are displayed in Fig 2. In this figure, we have only shown Q_{st} for stable states; i.e., for the three systems that exhibit hysteresis, the plot jumps from the vapor to liquid branches at the binodal. The resultant plots of Q_{st} are extraordinarily smooth compared to similar plots generated by conventional GCMC, particularly in the middle-density

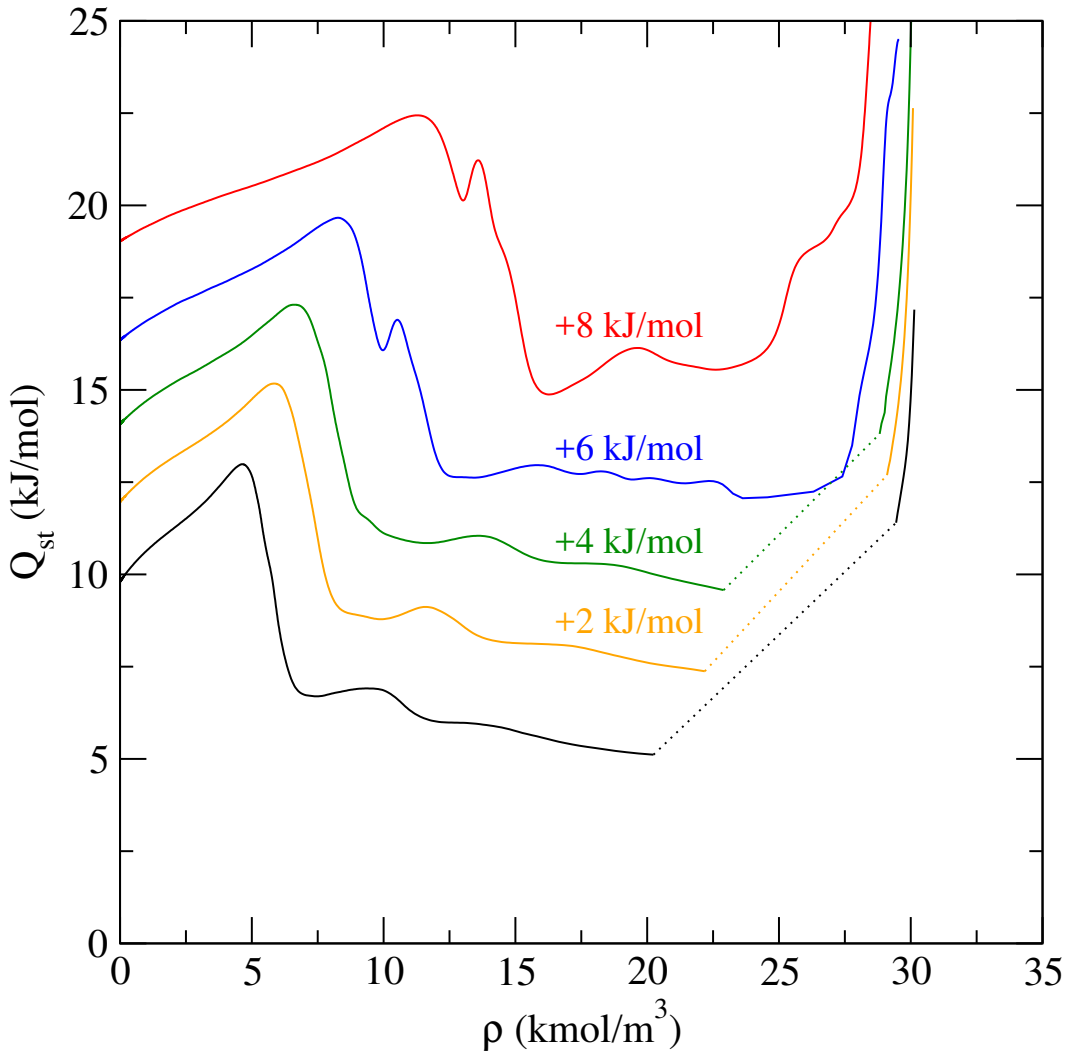

FIG. 3: Isosteric heat of adsorption (Q_{st}) for Ar-MWCNT systems computed at 87.3 K using GC-TMMC and eq YY plotted versus the average Ar density in the pore. Line colors correspond to radii as in Fig 2. All lines save that for $R = 3.935$ nm have been vertically shifted by the amount noted in the figure. The dotted lines are an aid to the eye that connect the stable vapor and stable liquid branches of Q_{st} for the three systems that exhibit hysteresis.

pore-filling region and on the liquid branches (e.g., see Fig 11 of Ref.[35]). This is likely due to GC-TMMC's use of the actual PNPD to compute the $f(U, N)$ and other fluctuation quantities, which must be computed using a well-tuned block averaging scheme in a conventional MC simulation. While these smoother Q_{st} results are unlikely to lead to qualitatively different conclusions than those from a conventional MC simulation, the removal of a significant amount of noise from Q_{st} calculations may make fine details more visible. For the case in Fig

3, the general shape of the Q_{st} curves is as expected, with a prominent peak at low density (corresponding to complete formation of the first adsorbed monolayer), largely unchanging Q_{st} as the pores infill, and a sharp rise when pore filling is complete. For the two smallest radii (those without hysteresis), Q_{st} contains a second high energy peak, which indicates that a second distinct monolayer has formed. (A second peak is present for the other radii, but at lower energy, indicating that the monolayer is more diffuse than the layer closest to the MWCNT surface.) This feature is not obvious in the isotherms for those radii and is a simple illustration of the extra insight obtained by calculation of Q_{st} in tandem with an adsorption isotherm.

We examined the statistical variation of adsorption properties of these Ar-MWCNT systems by analyzing the results of four repeat GC-TMMC simulations of the $R = 2.646$ nm system using appropriate statistical tests. Each independent batch of simulations (e.g., the set of simulations for the "divide and conquer" strategy) was initialized from a different configuration with a different seed integer for the random number generator and run as described above. Then, the adsorption analysis described in Section 2 was applied to the four PNPDs to yield the various adsorption properties described in the present text, after which we computed the 95 % confidence intervals for those properties to be used as estimates of the statistical uncertainty. Overall, the adsorption isotherms generated by GC-TMMC have very low uncertainties. We observe the largest relative uncertainties, up to 4.27 %, at very low p/p_0. For nominal pressures ($p/p_0 > 0.0005$), the relative uncertainty is of the order 0.1 % or smaller. Relative uncertainties for the p/p_0 locations of the equilibrium phase transition, vapor stability limit (capillary evaporation), and the liquid stability limit (capillary condensation) are 2.881×10^{-4}, 3.380×10^{-4}, and 1.084×10^{-3}, respectively. In all cases, the uncertainty in the location of these phase properties is low in both real and relative terms, as the relative uncertainties are less than 0.1 % at the equilibrium phase transition and condensation spinodal and still only 0.22 % at the evaporation spinodal. Lastly, we find that the relative uncertainty in the isosteric heat is somewhat larger than that in the properties already mentioned. The maximum uncertainty in Q_{st} was 1.300 kJ/mol at $\rho = 30.09$ kmol/m^3 ($p/p_0 = 0.9961$), corresponding to a relative error of 5.38 %; this is also the largest relative uncertainty observed in Q_{st}. For vapor densities, however, the maximum uncertainty was only 0.2684 kJ/mol and the maximum relative uncertainty (at a different p/p_0) was 3.58 %. An examination of the simulation data showed that the larger errors in

Q_{st} followed from larger variation in $U(N,V,T)$ at the highest density macrostates. Overall, the GC-TMMC method yields very consistent results across multiple simulations, leading to acceptable uncertainties in the adsorption properties computed from the PNPD and other ensemble averages.

B. Ar - MWCNT (2)

To demonstrate the consistency of GC-TMMC with conventional GCMC, we performed simulations of an Ar-MWCNT adsorptive system that was recently investigated by Wang et al.[35]. As mentioned previously, the MWCNT adsorbent was composed of three concentric CNT layers with interlayer spacing $\Delta = 0.3354$ nm[36], and the LJ and CLJ 10-4 potentials were used with the parameters in Table 1. The cylindrical radius was set to 2.20 nm and the axial length to 4.4 nm and the Ar-Ar interactions were cut and shifted at 2.20 nm, as in Ref. 35. GC-TMMC simulations were performed at $T = 87.3$ K with $N_{min} = 0$ and $N_{max} = 1350$ at $z\sigma_{Ar}^3 = 0.001708$ ($p = 53.38$ kPa, $p/p_0 = 0.5594$) to obtain $\Pi(N;\mu,V,T)$. The adsorption isotherm generated from the GC-TMMC PNPD is shown in Fig 4 along with the isotherm generated by conventional GCMC presented in Fig 12 of Ref.[35]. For both isotherms, the average density is based on the accessible volume definition of ρ using $R = 1.90$ nm as the accessible pore radius. The isotherm is very clearly a type IV isotherm with H1 hysteresis and, as in most simulations of smooth pores, shows distinct capillary phase transitions. Our GC-TMMC isotherm is in outstanding agreement with the conventional GCMC isotherm, save for the location of the capillary condensation transition and associated limit of stability which our GC-TMMC simulation predicts at a slightly higher pressure than the GCMC result. This difference is most likely due to the inherent challenges of simulating a fluid near a limit of stability, where the free energy barrier between two phases is extremely low. Despite this minor difference, the results confirm that the GC-TMMC method yields thermodynamic properties consistent with other simulation techniques.

C. Ar - CO_2

For additional validation of GC-TMMC, we now examine the adsorption of Ar in a cylindrical pore bored through solid CO_2, which was previously examined by Panagiotopoulos[37]

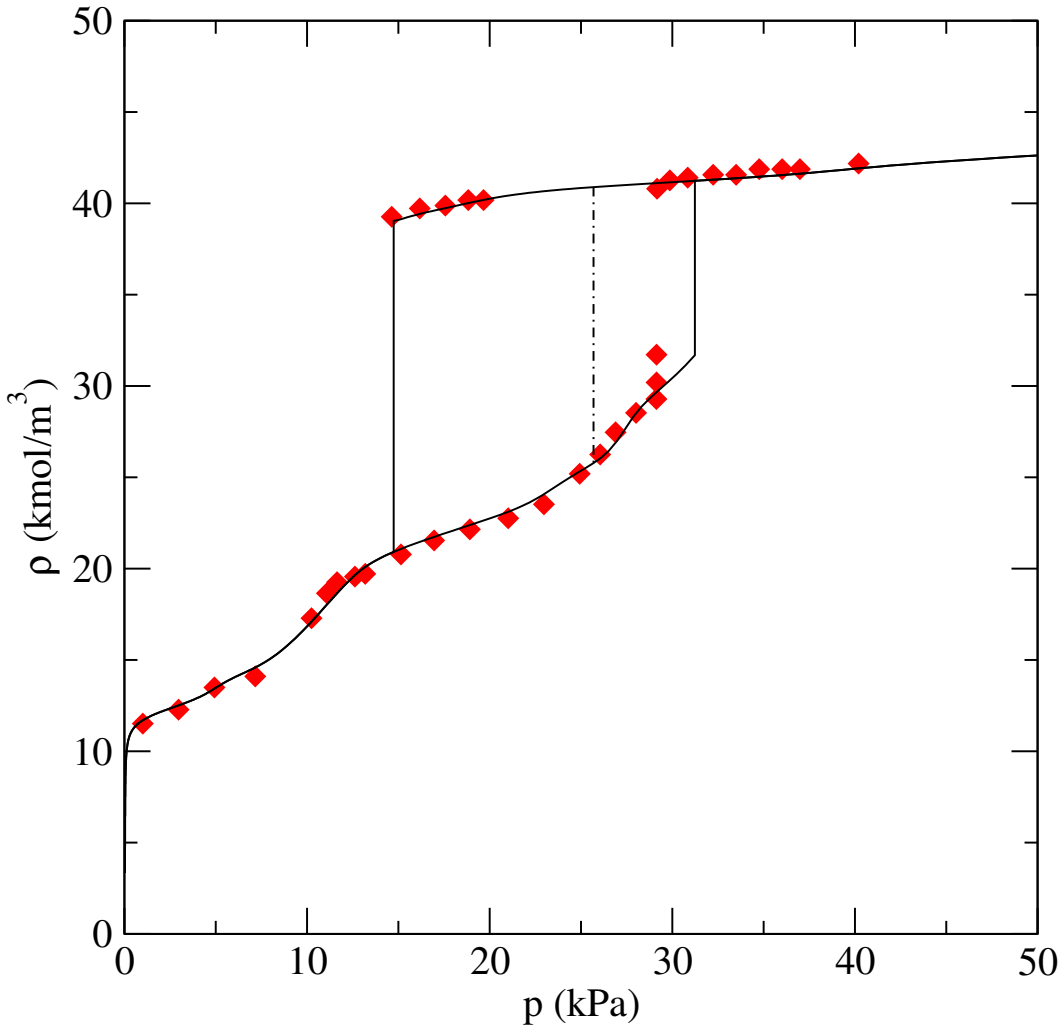

FIG. 4: Adsorption isotherm for Ar-MWCNT system with radius 2.2 nm computed at 87.3 K. The solid black line is the isotherm generated by the GC-TMMC described here. Red symbols are from the GC-MC simulations of Wang et al., from Fig 12 of Ref. 35. ρ is the average volume of Ar in the pore, based on the total volume definition and p is the gas pressure in units of kPa. The equilibrium phase transition for systems exhibiting hysteresis is shown by the black dashed line

using Gibbs ensemble MC. For this simulation, we model the adsorptive system using the LJ and CLJ 9-3 potentials mentioned earlier with the interaction parameters given in Table 1. To allow comparison of GC-TMMC results with those of Panagiotopoulos, we set $r_{cut} = 10\sigma_{Ar}$ and set the cylinder's radius to $3\sigma_{Ar} = 1.022$ nm and the axial length to $20\sigma_{Ar} = 6.810$ nm. We ran a GC-TMMC simulation with $N_{min} = 0$ and $N_{max} = 440$ at 95.8 K ($kT/\epsilon = 0.8$) and $z\sigma^3_{Ar} = 0.006392$ to obtain a $\Pi\left(N;\mu,V,T\right)$. The resultant isotherm

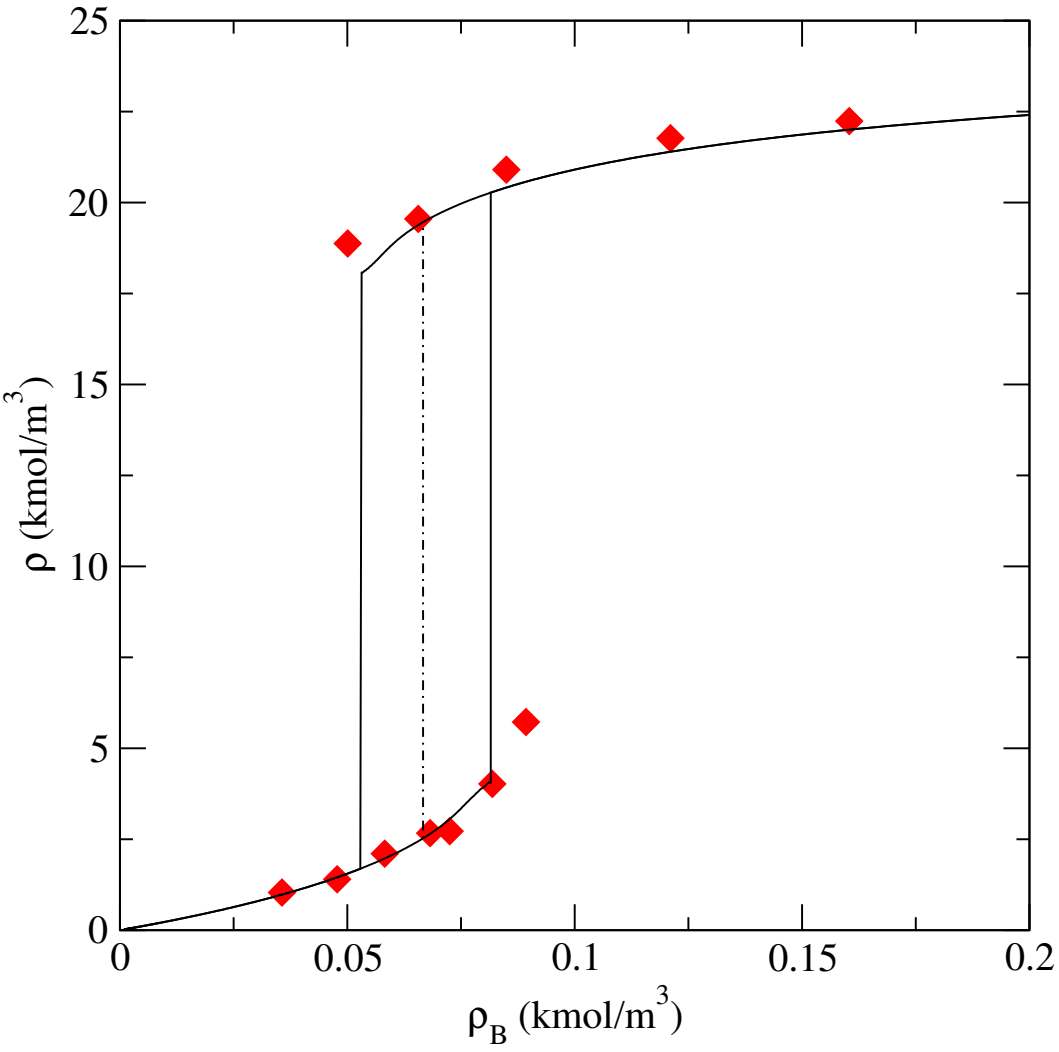

FIG. 5: Adsorption isotherm for Ar adsorbing in a cylindrical pore bored through solid CO_2 with radius 1.022 nm at 95.8 K. ρ is the average density of Ar in the pore, based on the total volume definition. ρ_B is the density of the bulk gas for the imposed μ, which was computed in an independent GC-TMMC simulation of the unconfined fluid[38]. The solid line is the isotherm computed using GC-TMMC and the dashed-dot line is the equilibrium phase transition. Red symbols are simulation points from Ref. 37 that were computed using Gibbs ensemble Monte Carlo simulation.

is plotted in Fig 5 along with points taken from Fig 7 of Ref. 37. For this isotherm, the average Ar density in the pore (based on the total volume definition) is plotted versus the bulk gas density, as in Ref. 37. The relationship between the bulk gas density and imposed chemical potential was obtained from an independent bulk fluid simulation of the LJ fluid

using long-range corrections (which will not differ greatly from those of the linear-force shift correction for $r_{cut} = 10\sigma_{Ar}$), the results of which are freely available on the NIST Standard Reference Simulation Website[38]. For the Ar-CO_2 system at 95.8 K, the resultant isotherm exhibits the classic type H1 hysteresis in the IUPAC classification scheme[39] with distinct vapor and liquid branches and vertical capillary phase transitions. The vapor branch of the isotherm is convex to the density (pressure) axis, which is indicative of the weak fluid-solid interaction of the CLJ 9-3 potential[40] and is similar to a type III isotherm[39]. We find that GC-TMMC nearly reproduces the Gibbs ensemble results of Panagiotopoulos with only minor differences. On the liquid branch of the isotherm, GC-TMMC yielded densities slightly below Panagiotopoulos' points, but by less than 2 %. This deviation is likely within the statistical error of both simulations. Additionally, the Gibbs ensemble results include two points beyond the limits of stability identified by GC-TMMC, one on each of the vapor and liquid branches. The appearance of these points may be attributed to the difficulty of the Gibbs ensemble to adequately sample phases separated by a low free energy barrier, such as near critical points and, in this case, near a limit of stability. We are inclined to ignore this small difference and find that the results are one validation of the GC-TMMC method for generating hysteretic adsorption isotherms.

Comparison with the results in Ref. 37 also offers an opportunity to evaluate our identification of the equilibrium phase transition, shown in Fig 5 by the dashed-dot line, since Panagiotopoulos computed the intrapore phase coexistence conditions using a "pore-pore" form of Gibbs ensemble MC. (Direct "pore-pore" equilibrium was possible in this case because the fluid-solid interaction was independent of the system length, allowing for straightforward volume exchange moves. This approach would not be possible for a rigid, atomistically detailed adsorbent which does not allow for volume exchange moves.) In Fig 7 of Ref. 37, the coexisting densities at the equilibrium phase transition are, approximately, $\rho_v\sigma^3 = 0.059$ and $\rho_l\sigma^3 = 0.46$ (corresponding to 0.63 and 19.3 kmol/m^3, respectively). Our GC-TMMC simulation yielded coexistence densities of $\rho_v\sigma^3 = 0.06009(2)$ and $\rho_l\sigma^3 = 0.4626(1)$. The number in parentheses is the uncertainty in the last digit estimated from 95% confidence intervals based on four replicate GC-TMMC simulations with differing initial configurations. Our calculations of the phase coexistence densities are essentially indistinguishable from the Gibbs ensemble results of Ref 37. For completeness, we note that the equilibrium phase transition for the Ar-CO_2 system occurs at $\rho_B\sigma^3 = 0.0015850(4)$ or $p/p_0 = 0.26942(6)$. The

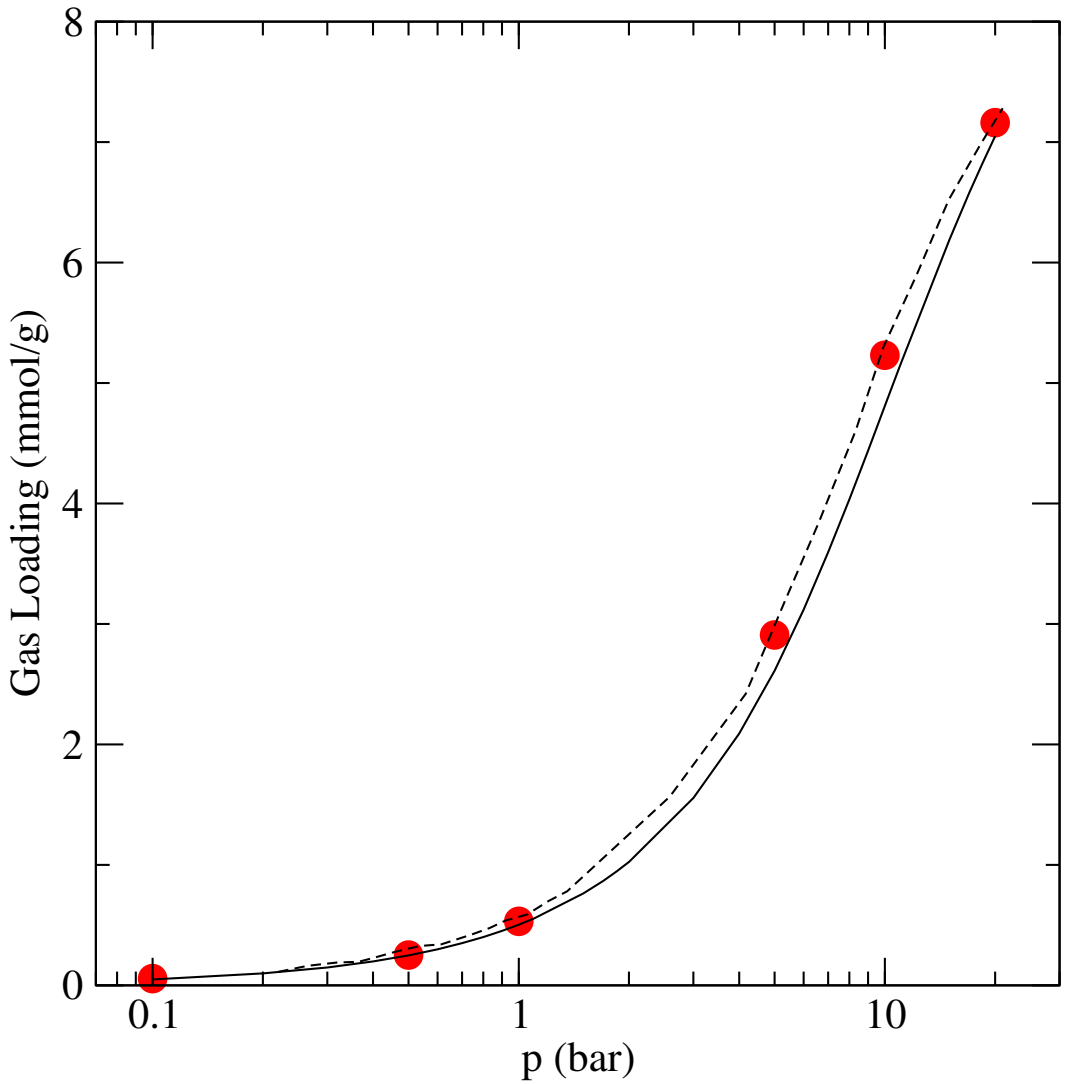

FIG. 6: Adsorption isotherm for CO_2 in ZIF-8 at 303 K plotted versus imposed pressure. The loading value is absolute adsorption of CO_2 per unit weight ZIF-8 adsorbent. p, given in bar, is the pressure for the imposed μ, which was computed by a GC-TMMC of unconfined CO_2. The solid black line is the isotherm computed here using GC-TMMC. Red symbols are MC simulation points from Figs 2 and 3 of Ref. 41. The black dashed line is an experimental isotherm given in the same figures of Ref. 41.

agreement between our GC-TMMC simulations and earlier Gibbs ensemble MC simulations serves as a confirmation that the two methods yield essentially identical results.

D. CO_2 Adsorption in ZIF-8

Lastly, as a demonstration of the ability of GC-TMMC to model adsorption of a more complicated gas than Ar, we now examine the adsorption of CO_2 by the metal-organic framework ZIF-8, which has been considered as a prospective material for carbon capture applications[41,42]. This application of GC-TMMC represents a more challenging case than the two Ar examples already discussed, since the TraPPE model of CO_2 contains multiple LJ sites and point charges, which necessitate the CBMC and Ewald summation methods mentioned previously. Figure 6 contains the adsorption isotherm obtained via GC-TMMC at 303 K along with both simulation and experimental results from Ref. 41. We note that the authors of Ref. 41 used the EPM-2 model of CO_2[43], which differs from the TraPPE model in its interaction parameters. The resultant isotherm from GC-TMMC is a type I Langmuir-like isotherm[39], which is expected since the temperature is just below the critical temperature of CO_2 (approximately 306.2 K for TraPPE CO_2[44], only slightly above that reported for real CO_2, 304.1-304.4 K). This general isotherm trend is identical to the experimental and simulation isotherms reported in Ref. 41 and our isotherm is essentially indistinguishable from those results up to $p = 1$ bar. For larger pressures, the TraPPE isotherm is slightly lower (5 % to 10 %) compared to both the experimental and EPM-2 isotherms from 1 bar to 20 bar. This is expected since the LJ parameters of EPM-2 CO_2 are slightly stronger than those of TraPPE CO_2 and due to the enhanced packing made possible by the slightly smaller EPM-2 structure. We point out once again that the GC-TMMC isotherm shown in Fig 6 was obtained from a single molecular simulation and that the PNPD could be reweighted to yield additional isotherm points if desired.

IV. SUMMARY AND CONCLUSIONS

In this work, we introduced a GC-TMMC method as an efficient technique for computing various properties of an adsorbed fluid for situations where multiple fluid phases, both stable and metastable, may be present. The key statistical quantity exploited in this work is the PNPD, which is straightforwardly obtained from information about attempted transitions in an otherwise normal MC simulation. The TMMC method selected here is that of Errington and co-workers, which is distinguished from earlier TMMC work by the introduction of

a biasing function proportional to the logarithm of the aforementioned PNPD. The self-correcting biasing function encourages the simulation to sample all states uniformly, allowing for satisfactory sampling of N-states with both low and high probability and the accurate construction of the entire PNPD, from which any number of ensemble averages can then be computed.

A particularly attractive feature of GC-TMMC is that a single simulation can provide the necessary information to generate various properties of the adsorptive system for any number of thermodynamic state points. Thus, the PNPD from a single simulation is able to generate an entire adsorption isotherm, locate capillary phase transitions, identify the equilibrium phase transition, and compute other properties. The example applications that we discussed in Sec 3 demonstrate that the GC-TMMC method generates adsorption isotherms that are consistent with both expected behavior of adsorbed fluids and with previously published simulation results generated by conventional GCMC and Gibbs ensemble simulations of fluid confined in adsorbing pores. Additionally, we demonstrated the ability of GC-TMMC to compute other properties of adsorbed fluids by computing the isosteric heat of adsorption. This property is more challenging to reliably calculate than simple ensemble averages as it is computed from ensemble fluctuations. The Q_{st} results given here for a family of Ar-MWCNT systems appear to contain less noise than calculations in existing GCMC simulations, which likely follows from the use of the PNPD to compute the necessary ensemble fluctuations.

A valid question that may be asked is whether the GC-TMMC method presents a computational advantage to conventional GCMC, since a particular GC-TMMC simulation is typically run for many more trial moves than an equivalent GCMC simulation. While it is true that one GC-TMMC simulation might require more computational time than, say, the 20 or 50 conventional GCMC simulations used to generate an adsorption isotherm, it is important to keep in mind that a single GC-TMMC simulation provides access to the continuum of state points comprising the entire curve, which is the equivalent of hundreds or thousands of individual GCMC simulations.

The work here presents an initial application of the GC-TMMC method to adsorption problems involving hysteresis and we anticipate that this method can be widely exploited to improve modeling of adsorption and obtain properties that might be difficult to obtain with conventional or more established forms of MC simulation. For example, if an adsorptive system could support more than two stable states, it is possible that existing MC methods

might fail to identify some of those states. In other applications, one can consider the use of temperature-expanded ensembles[45–47] and/or temperature reweighting[26] of a macrostate probability distribution to obtain additional temperature-dependent information from a GC-TMMC simulation. This might be used to rigorously search for the hysteresis critical temperature or simply to compute adsorption isotherms and associated properties for more than one temperature, all from a single simulation. Also, since GC-TMMC falls into the class of flat histogram simulation methods, it is possible to combine its algorithm with other flat histogram strategies to further improve its efficiency. One such approach is that suggested by Shell et al.[48] in which the Wang-Landau method[48–51] is used to quickly generate the biasing potential while using GC-TMMC to compute the PNPD. Finally, though the present discussion involved fairly simple fluid models (single-site LJ Ar and rigid multisite CO_2), GC-TMMC is no less suited to more complicated fluid models and advanced MC sampling strategies, and modeling of adsorption of complex fluids in various media is just another application that can be considered.

Acknowledgments

D.W.S. acknowledges the financial support from a National Research Council postdoctoral research associateship at the National Institute of Standards and Technology.

---

† Electronic address: daniel.siderius@nist.gov

[1] Gelb, L. D.; Gubbins, K. E.; Radhakrishnan, R.; Sliwinska-Bartkowiak, M. Phase separation in confined systems. *Rep. Prog. Phys.* **1999**, *62*, 1573–1659.

[2] Rouquerol, F.; Rouquerol, J.; Sing, K. *Adsorption by Powders and Porous Solids*; Academic Press: London, 1999.

[3] Lowell, S.; Shields, J. E.; Thomas, M. A.; Thommes, M. *Characterization of porous solids and powders: Surface area, pore size and density*; Kluwer: Boston, 2004.

[4] Khoo, H. H.; Tan, R. B. H. Life Cycle Investigation of CO_2 Recovery and Sequestration. *Environ. Sci. Technol.* **2006**, *40*, 4016–4024.

[5] Maginn, E. J. What to do with CO_2. *J. Phys. Chem. Lett.* **2010**, *1*, 3478–3479.

[6] Meek, S. T.; Greathouse, J. A.; Allendorf, M. D. Metal-Organic Frameworks: A Rapidly Growing Class of Versatile Nanoporous Materials. *Adv. Mater.* **2010**, *23*, 249–267.

[7] Zhou, H. C.; Long, J. R.; Yaghi, O. M. Introduction to Metal Organic Frameworks. *Chem. Rev.* **2012**, *112*, 673–674.

[8] Gubbins, K. E.; Liu, Y. C.; Moore, J. D.; Palmer, J. C. The role of molecular modeling in confined systems: Impact and prospects. *Phys. Chem. Chem. Phys.* **2011**, *13*, 58–85.

[9] Monson, P. A. Understanding adsorption/desorption hysteresis for fluids in mesoporous materials using simple molecular models and classical density functional theory. *Microporous Mesoporous Mater.* **2012**, *160*, 47–66.

[10] Yang, Q.; Xue, C.; Zhong, C.; Chen, J. F. Molecular simulation of separation of CO2 from flue gases in CU-BTC metal-organic framework. *AIChE J.* **2007**, *53*, 2832–2840.

[11] Watanabe, S.; Sholl, D. S. Accelerating applications of metal-organic frameworks for gas adsorption and separation by computational secreening of materials. *Langmuir* **2012**, *28*, 14114–14128.

[12] Lin, L. C.; Berger, A. H.; Martin, R. L.; Kim, J.; Swisher, J. A.; Jariwala, K.; Rycroft, C. H.; Bhown, A. S.; Deem, M. W.; Haranczyk, M.; Smit, B. In silico screening of carbon-capture materials. *Nat. Mater.* **2012**, *11*, 633–641.

[13] Evans, R. Density Functionals in the Theory of Nonuniform Fluids. In *Fundamentals of Inhomogeneous Fluids*; Henderson, D., Ed.; Dekker: New York, 1992; pp 85–175.

[14] de Oliveira, M. J.; Griffiths, R. B. Lattice-gas model of multiple layer adsorption. *Surf. Sci.* **1978**, *71*, 687–694.

[15] Marconi, U. M. B.; van Swol, F. Microscopic model for hysteresis and phase equilibria of fluids confined between parallel plates. *Phys. Rev. A* **1989**, *39*, 4109–4116.

[16] Kierlik, E.; Monson, P. A.; Rosinberg, M. L.; Sarkisov, L.; Tarjus, G. Capillary condensation in disordered porous materials: Hysteresis versus equilibrium behavior. *Phys. Rev. Lett.* **2001**, *87*, 055701.

[17] Siderius, D. W.; Gelb, L. D. Predicting gas adsorption in complex microporous and mesoporous materials using a new density functional theory of finely discretized lattice fluids. *Langmuir* **2009**, *25*, 1296–1299.

[18] Allen, M. P.; Tildesley, D. J. *Computer Simulation of Liquids*; Clarendon: New York, 1987.

[19] Frenkel, D.; Smit, B. *Understanding Molecular Simulation*; Academic Press: San Diego, CA, 1996.

[20] Sarkisov, L.; Monson, P. A. Modeling of adsorption and desorption in pores of simple geometry using molecular dynamics. *Langmuir* **2001**, *17*, 7600–7604.

[21] Neimark, A. V.; Ravikovitch, P. I. Adsorption hysteresis in nanopores. *Phys. Rev. E* **2000**, *62*, R1493–R1496.

[22] Neimark, A. V.; Ravikovitch, P. I. Capillary condensation in MMS and pore structure characterization. *Microporous Mesoporous Mater.* **2001**, *44-45*, 697–707.

[23] Fitzgerald, M.; Picard, R. R.; Silver, R. N. Canonical transition probabilities for adaptive Metropolis simulation. *Europhys. Lett.* **1999**, *46*, 282–287.

[24] Fitzgerald, M.; Picard, R. R.; Silver, R. N. Monte Carlo transition dynamics and variance reduction. *J. Stat. Phys.* **2000**, *98*, 321–345.

[25] Errington, J. R. Evaluating surface tension using grand-canonical transition-matrix Monte Carlo simulation and finite-size scaling. *Phys. Rev. E* **2003**, *67*, 012102.

[26] Errington, J. R. Direct calculation of liquid-vapor phase equilibria from transition matrix Monte Carlo simulation. *J. Chem. Phys.* **2003**, *118*, 9915–9925.

[27] Shen, V. K.; Errington, J. R. Metastability and instability in the Lennard-Jones fluid investigated by transition-matrix Monte Carlo. *J. Phys. Chem. B* **2004**, *108*, 19595–19606.

[28] Shen, V. K.; Errington, J. R. Determination of fluid-phase behavior using transition-matrix Monte Carlo: Binary Lennard-Jones mixtures. *J. Chem. Phys.* **2005**, *122*, 064508.

[29] Errington, J. R.; Shen, V. K. Direct evaluation of multicomponent phase equilibria using flat-histogram methods. *J. Chem. Phys.* **2005**, *123*, 164103.

[30] Shen, V. K.; Errington, J. R. Determination of surface tension in binary mixtures using transition-matrix Monte Carlo. *J. Chem. Phys.* **2006**, *124*, 024721.

[31] Mohr, P. J.; Taylor, B. N.; Newell, D. B. CODATA recommended values of the fundamental physical constants: 2010. *Rev. Mod. Phys.* **2012**, *84*, 1527–1605.

[32] Metropolis, N.; Rosenbluth, A.; Rosenbluth, M. N.; Teller, A.; Teller, E. Equation of state calculations by fast computing machines. *J. Chem. Phys.* **1953**, *21*, 1087–1092.

[33] Hastings, W. K. Monte Carlo sampling methods using Markov chains and their applications. *Biometrika* **1970**, *57*, 97–109.

[34] Frey, J. T.; Doren, D. J. *Tubegen 3.4*, 2011. `http://turin.nss.udel.edu/research/tubegenonline.html`.

[35] Wang, Y.; Do, D. D.; Nicholson, D. Study of heat of adsorption across the capillary condensation

in cylindrical pores. *Colloids Surf. A* **2011**, *380*, 66–78.

[36] Wang, Y. and Do, D. D., , Personal Communication, 2012. In Ref. 35, the CNT adsorbent was composed of three concentric CNTs, which was not specified in the text.

[37] Panagiotopoulos, A. Z. Adsorption and capillary condensation of fluids in cylindrical pores by Monte-Carlo simulation in the Gibbs ensemble. *Mol. Phys.* **1987**, *62*, 701–719.

[38] *NIST Standard Reference Simulation Website.* `http://doi.org/10.18434/T4M88Q`, NIST Standard Reference Database 173.

[39] Sing, K. S. W.; Everett, D. H.; Haul, R. A. W.; Moscou, L.; Pierotti, R. A.; Rouquerol, J.; Siemieniewska, T. Reporting physisorption data for gas/solid systems with special reference to the determination of surface area and porosity. *Pure Appl. Chem.* **1985**, *57*, 603–619.

[40] Siderius, D. W.; Gelb, L. D. Extension of the Steele 10-4-3 potential for adsorption calculations in cylindrical, spherical, and other pore geometries. *J. Chem. Phys.* **2011**, *135*, 084703.

[41] Perez-Pellitero, J.; Amrouche, H.; Siperstein, F. R.; Pirngruber, G.; Nieto-Draghi, C.; Chaplais, G.; Simon-Masseron, A.; Bazer-Bachi, D.; Peralta, D.; Bats, N. Adsorption of CO_2, CH_4, and N_2 on zeolitic imidazolate frameworks: Experiments and simulations. *Chem.-Eur. J.* **2010**, *16*, 1560–1570.

[42] Wong-Ng, W.; Kaduk, J. A.; Espinal, L.; Suchomel, M. R.; Allen, A. J.; Wu, H. High-resolution synchrotron X-ray powder diffraction study of bis(2-methylimidazolyl)-zinc, C8H10N4Zn (ZIF-8). *Powder Diffr.* **2011**, *26*, 234–237.

[43] Harris, J. G.; Yung, K. W. Carbon dioxide's liquid-vapor coexistence curve and critical properties as predicted by a simple molecular model. *J. Phys. Chem.* **1995**, *99*, 12021–12024.

[44] Potoff, J. A.; Siepmann, J. I. Vapor-liquid equilibria of mixtures containing alkanes, carbon dioxide, and nitrogen. *AIChE J.* **2001**, *47*, 1676–1682.

[45] Lyubartsev, A. P.; Martsinovski, A. A.; Shevkunov, S. V.; Vorontsov-Velyaminov, P. N. New approach to Monte Carlo calculation of the free energy: Method of expanded ensembles. *J. Chem. Phys.* **1991**, *96*, 1776–1783.

[46] Grzelak, E. M.; Errington, J. R. Nanoscale limit to the applicability of Wenzel's equation. *Langmuir* **2010**, *26*, 13297–13304.

[47] Kumar, V.; Sridhar, S.; Errington, J. R. Monte Carlo simulation strategies for computing the wetting properties of fluids at geometrically rough surfaces. *J. Chem. Phys.* **2011**, *135*, 184702.

[48] Shell, M. S.; Debenedetti, P. G.; Panagiotopoulos, A. Z. An improved Monte Carlo method for

direct calculation of the density of states. *J. Chem. Phys.* **2003**, *119*, 9406–9411.

[49] Wang, F.; Landau, D. P. Efficient, multiple-range random walk algorithm to calculate the density of states. *Phys. Rev. Lett.* **2001**, *86*, 2050–2053.

[50] Wang, F.; Landau, D. P. Determining the density of states for classical statistical models: A random walk algorithm to produce a flat histogram. *Phys. Rev. E* **2001**, *64*, 056101.

[51] Shell, M. S.; Debenedetti, P. G.; Panagiotopoulos, A. Z. Generalization of the Wang-Landau method for off-lattice simulations. *Phys. Rev. E* **2002**, *66*, 056703.